Human Molecular Genetics, 2018, Vol. 27, No. 22 3936–3950

doi: 10.1093/hmg/ddy292
Advance Access Publication Date: 9 August 2018
General Article

GENERAL ARTICLE

Fragile X mental retardation protein modulates the stability of its m^{6}A-marked messenger RNA targets

Feiran Zhang[1], Yunhee Kang[1], Mengli Wang[1], Yujing Li[1], Tianlei Xu[2], Wei Yang[3], Hongjun Song[4], Hao Wu[2], Qiang Shu[5] and Peng Jin[1,*]

[1]Department of Human Genetics, Emory University School of Medicine, Atlanta, GA 30322, USA, [2]Department of Biostatistics and Bioinformatics, Emory University Rollins School of Public Health, Atlanta, GA 30322, USA, [3]Department of Neurology, The Second Hospital of Jilin University, Changchun, Jilin 130041, China, [4]Department of Neuroscience, Mahoney Institute for Neurosciences, Institute for Regenerative Medicine and The Epigenetics Institute, Perelman School for Medicine, University of Pennsylvania, Philadelphia, PA 19104, USA and [5]The Children's Hospital and Institute of Translational Medicine, School of Medicine, Zhejiang University, Hangzhou, Zhejiang 310029, China

*To whom correspondence should be addressed. Tel: +1 404 727 3729; Fax: +1 404 727 5408; Email: peng.jin@emory.edu

Abstract

N^6-methyladenosine (m^{6}A) is the most prevalent internal modification of mammalian messenger RNAs (mRNAs) and long non-coding RNAs. The biological functions of this reversible RNA modification can be interpreted by cytoplasmic and nuclear 'm^{6}A reader' proteins to fine-tune gene expression, such as mRNA degradation and translation initiation. Here we profiled transcriptome-wide m^{6}A sites in adult mouse cerebral cortex, underscoring that m^{6}A is a widespread epitranscriptomic modification in brain. Interestingly, the mRNA targets of fragile X mental retardation protein (FMRP), a selective RNA-binding protein, are enriched for m^{6}A marks. Loss of functional FMRP leads to Fragile X syndrome (FXS), the most common inherited form of intellectual disability. Transcriptome-wide gene expression profiling identified 2035 genes differentially expressed in the absence of FMRP in cortex, and 92.5% of 174 downregulated FMRP targets are marked by m^{6}A. Biochemical analyses indicate that FMRP binds to the m^{6}A sites of its mRNA targets and interacts with m^{6}A reader YTHDF2 in an RNA-independent manner. FMRP maintains the stability of its mRNA targets while YTHDF2 promotes the degradation of these mRNAs. These data together suggest that FMRP regulates the stability of its m^{6}A-marked mRNA targets through YTHDF2, which could potentially contribute to the molecular pathogenesis of FXS.

Introduction

Epigenetic regulation has been shown to play pivotal roles in the development and functions of central nervous system. N^6-methyladenosine (m^{6}A) is the most prevalent internal modif ication of mammalian messenger RNAs (mRNAs) and long non-coding RNAs (lncRNAs) (1). A multi-component methyltransferase complex containing several subunits (METTL3, METTL14, WTAP, KIAA1429/VIRMA, RBM15 and RBM15B) installs m^{6}A (2–6). Two demethylases of the AlkB dioxygenase family, FTO and ALKBH5, remove m^{6}A (7,8). The biological functions of this dynamic RNA modification can be interpreted by many cytoplasmic and nuclear proteins (known as 'm^{6}A readers') to fine-tune multiple steps in RNA life cycle, such as nuclear pre-mRNA splicing (YTHDC1 and HNRNPA2/B1), nuclear export of mRNA (YTHDC1), microRNA generation (HNRNPA2/B1), translation initiation (YTHDF1, YTHDF3, YTHDC2 and eIF3) and

Received: April 4, 2018. **Revised:** July 17, 2018. **Accepted:** August 7, 2018

mRNA degradation (YTHDF2 and YTHDC2) (9–19). In addition, m^{6}A can change the accessibility of its surrounding sequence by altering the local structures in mRNAs and lncRNAs, thus modulate the interaction between RNA and RNA binding proteins (a mechanism known as 'm^{6}A-switch') (20,21). m^{6}A is particularly abundant in mammalian brain and the methylome is conserved in mammals (22,23). We and others have revealed prominent functions of m^{6}A methylase and demethylase in the proliferation and differentiation of adult neural stem cells, cortical neurogenesis, hippocampal learning and memory, midbrain dopaminergic signaling and circadian clock control (24–28).

Fragile X syndrome (FXS, OMIM#300624) is the most common inherited form of intellectual disability and a leading genetic cause of autism spectrum disorders (ASD) (29–31). FXS is caused by loss of functional fragile X mental retardation protein (FMRP) (32). FMRP, encoded by *FMR1* gene, is a selective RNA-binding protein associated with translating polyribosomes (polysome) (33–35). It represses and regulates translation of a set of synaptic plasticity-related transcripts. Coinciding with m^{6}A, FMRP is also particularly abundant in brain with high expression in neurons. Intriguingly, the consensus sequence for m^{6}A methylation, RGACH (R = A/G; H = A or C/U) largely overlaps with FMRP-bound YGGA (Y = C/U) and GAC motifs and is found in 57% of FMRP consensus binding sites (22,23,36–38). Furthermore, FMRP has recently been shown to bind an m^{6}A-containing RNA probe $(GGACU)_4$ (39).

In this study, we determined the transcriptome-wide m^{6}A sites in adult mouse cerebral cortex using anti-m^{6}A RNA immunoprecipitation (RIP) followed by high-throughput sequencing (m^{6}A-seq). We found that the mRNA targets of FMRP are significantly enriched for m^{6}A marks, and the loss of FMRP alters both transcriptome and epitranscriptome in cortex. Surprisingly, among FMRP targets, at least 92% of *Fmr1* KO-downregulated mRNAs were marked by m^{6}A [with an odds ratio (OR) near 7], suggesting that FMRP could have interplay with m^{6}A-mediated regulation of mRNA stability. Our biochemical analyses indicated that FMRP could bind to m^{6}A sites in its targets and interact with YTHDF2, an 'm^{6}A reader', in an RNA-independent manner. Functionally, we showed that FMRP maintains the stability of its mRNA targets while YTHDF2 promotes the degradation of these transcripts. Together, our works demonstrate that FMRP regulates the stability of its mRNA targets marked by m^{6}A, most likely through YTHDF2. This mechanism represents an additional layer of gene regulation mediated by FMRP, which could potentially contribute to the molecular pathogenesis of FXS.

Results

m^{6}A RNA methylation is a widespread mRNA modification in mouse cerebral cortex

To determine the landscape of m^{6}A in mammalian brain, we profiled the transcriptome-wide m^{6}A sites in the cerebral cortex of 6 week old male mice using m^{6}A-seq (Supplementary Material, Fig. S1A) (28,40). Poly(A)(+) RNA isolated from cortex tissue of six mice were pooled for each assay. m^{6}A-seq identified about 22 000 genome-based peaks (false discovery rate, FDR, < 0.001) shared between two biological replicates as high-confidence m^{6}A peaks (or 'HC peaks') and 7587 mRNAs and ncRNAs as m^{6}A-marked transcripts (Supplementary Material, Fig. S1B and C and Table S1), suggesting that m^{6}A is a widespread regulatory mechanism for transcripts in adult cortex. In total 93% of HC peaks occur within genic regions (Fig. 1A), which are abundant in exons (75%), and highly enriched for 3' untranslated region (UTR) (38-fold), coding sequences (CDS) (36-fold) and 5' UTR (25-fold). In addition, a deduced consensus motif, RGACH (R = A/G; H = A or C/U), was greatly enriched in the HC peaks (Fig. 1B). Two variants of this consensus motif, WGGACH (W = A or U) and RGACU, were both centrally enriched within peaks (Supplementary Material, Fig. S1D). Intriguingly, FMRP target transcripts are significantly enriched for m^{6}A marks. About three quarters of 822 stably expressed FMRP targets (36) (Fragments Per Kilobase of transcript per Million mapped reads, or FPKM, ≥ 0.2) contained at least one HC peak (Fig. 1C, and Supplementary Material, Tables S1 and S2), insinuating that FMRP may directly bind to the m^{6}A sites in its targets as recently suggested by two research groups (39,41), and/or m^{6}A pathway and FMRP may potentially regulate the same set of genes. Overall, m^{6}A marks moderately expressed transcripts (23) and FMRP target transcripts marked by m^{6}A were expressed at lower levels than FMRP target transcripts with no m^{6}A peak (Fig. 1D), suggesting that the significant overlap between m^{6}A-marked transcripts identified by m^{6}A-seq and FMRP targets identified by high-throughput sequencing of RNAs isolated by crosslinking immunoprecipitation (HITS-CLIP) is not predominantly based on transcript abundance. Moreover, gene ontology (GO) analyses indicate that m^{6}A-marked FMRP targets are significantly enriched for GO terms related to nervous system development, synaptic transmission, intracellular signal transduction, learning and behaviors (Fig. 1E).

Loss of FMRP alters m^{6}A landscape in mouse cerebral cortex

Given the potential link between FMRP and m^{6}A pathway, we then investigated potential role(s) of FMRP in cortical m^{6}A epitranscriptome using *Fmr1* knockout (KO) mice. We performed m^{6}A-seq on two biological replicates of pooled poly(A)(+) RNA isolated from the cortex tissue of 6 week old males. m^{6}A-seq in KO cortex identified about 21 000 HC peaks as m^{6}A sites, and 7590 mRNAs and ncRNAs as m^{6}A-marked transcripts (Supplementary Material, Fig. S2A and B, and Table S1), close to those numbers in wild-type (WT) cortex. In addition, top two enriched motifs, WGGAC and AVAGACU (V = A/G or C), in the HC peaks from KO cortex were both centrally enriched within peaks and overlapped greatly with the WT motifs (Supplementary Material, Fig. S2C and D).

Next, we compared the m^{6}A peaks identified in WT and *Fmr1* KO cortex. About 14 000 HC peaks were present in all four m^{6}A-seq datasets from either WT or KO cortex (defined as common peaks) (Fig. 2A and Supplementary Material, Table S1). However, 2858 peaks were found only in WT cortex but not in any replicate of KO cortex (defined as WT-specific peaks), while 2769 peaks were found only in KO but not in any replicate of WT (defined as KO-specific peaks) (Fig. 2A–C, Supplementary Material, Fig. S2E–G and Table S1). Like most RIP-based experiments, m^{6}A signal detection relies on transcripts expressed at sufficient level. We compared the expression levels of 2016 transcripts marked by WT-specific peaks in WT and KO cortex and found that only < 14% of these transcripts were significantly downregulated in KO cortex (Supplementary Material, Fig. S2H, and Tables S1 and S2). Similarly, among 1143 transcripts containing KO-specific peaks, < 14% were significantly upregulated by *Fmr1* KO in cortex (Supplementary Material, Fig. S2H and Tables S1 and S2). These findings indicate that the majority of WT- and KO-specific peaks identified by

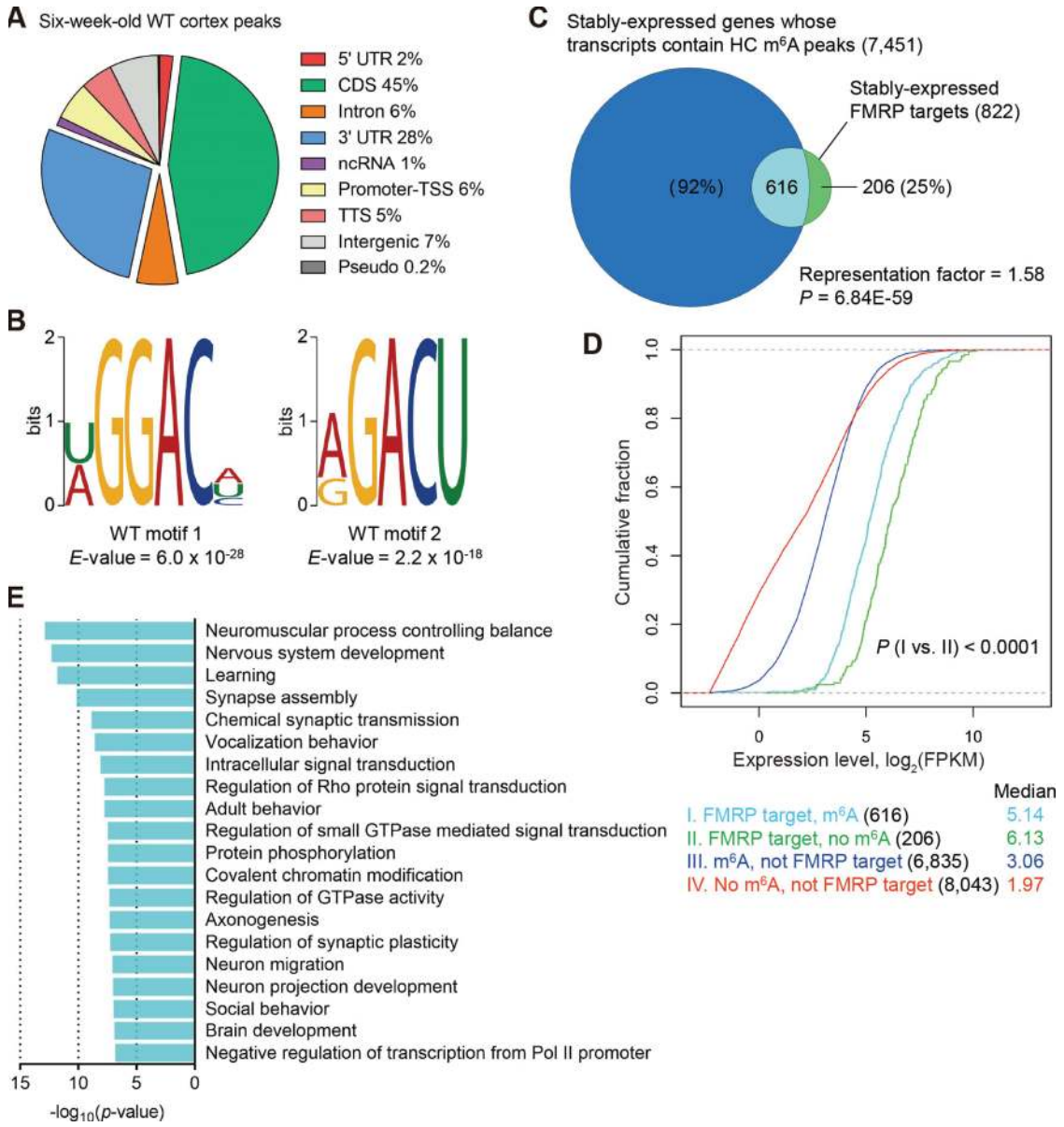

Figure 1. The mRNA targets of FMRP are significantly enriched for m^{6}A marks in cerebral cortex. **(A)** Pie chart illustrating the region distribution of HC peaks identified by m^{6}A-seq in 6 week old WT male mouse cortex; promoter-TSS, from −1 kb to +100 bp of transcription starting site (TSS); TTS, from −100 bp to + 1 kb of TTS; 5' UTR, from +101 bp of TSS to −1 bp of start codon; CDS from start codon to stop codon; 3' UTR, from +1 bp of stop codon to −101 bp of TTS; ncRNA, non-coding RNA; pseudo, pseudogene. **(B)** Top two enriched motifs identified by DREME tools with HC peaks from WT cortex. The un-erased *E*-value of each motif is shown. Out of top 988 scored peaks, 504 and 331 sites were found under WT motifs 1 and 2, respectively. **(C)** A significant overlap of genes containing HC peaks in WT cortex and genes encoding FMRP targets. Total number of stably expressed genes (FPKM ≥ 0.2) in WT cortex was 15 705. Chi-square test. **(D)** Cumulative distribution function plot of the expression levels of stably expressed cortical transcripts in different sectors shown in (C). Transcripts were grouped and color-coded based on their sectors. The numbers of transcripts in each sector are shown in parentheses. Two-tailed Mann–Whitney *U*-test. **(E)** GO analysis of stably expressed FMRP mRNA targets containing m^{6}A sites in WT cortex. Top 20 enriched biological processes are shown.

our m^{6}A-seq experiments were not due to altered transcript abundance. In addition, we noticed that the expression levels of transcripts marked by WT-specific peaks and by common peaks were overall very close to each other in both WT and KO cortex, but the transcripts marked by KO-specific peaks in general were expressed at lower level than the transcripts marked by common peaks in both WT and KO cortex (Fig. 2D). Finally, there were 2016 and 1143 genes whose transcripts were marked by WT- and KO-specific m^{6}A peaks, respectively (Fig. 2E and F). These two groups of genes overlapped significantly with stably expressed FMRP targets (Supplementary Material, Fig. S2I). Taken together, these results suggested that the loss of FMRP in cortex could alter m^{6}A epitranscriptome.

Loss of FMRP leads to the downregulation of long m^{6}A-marked FMRP targets

We next investigated how the loss of FMRP could impact on its targets marked by m^{6}A. Since FMRP is a polyribosome-associated RNA-binding protein (33,36), we applied MeTPeak (42) and MeTDiff (43) to identify exome-based m^{6}A peaks in mature transcripts

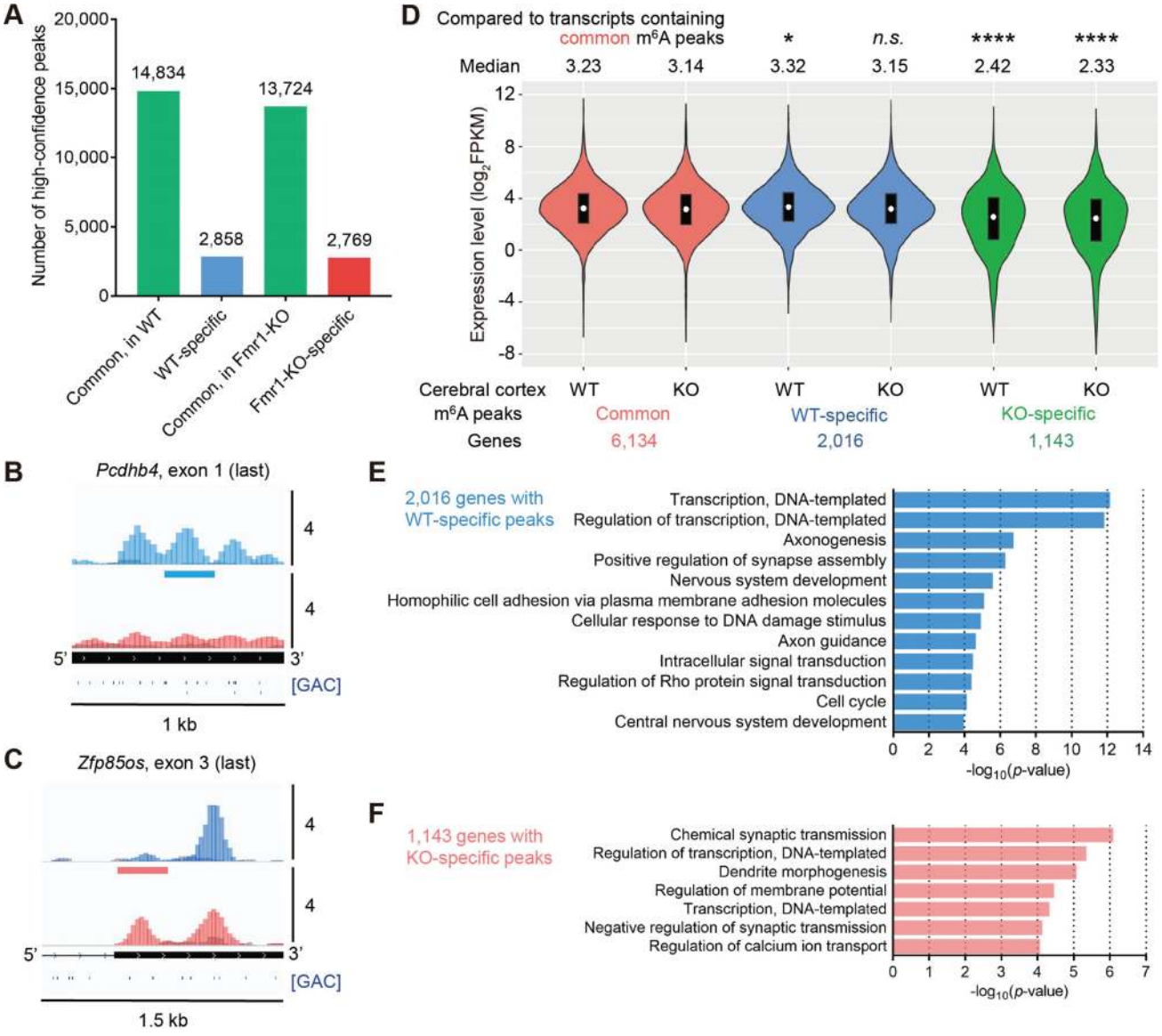

Figure 2. Loss of FMRP leads to altered m^{6}A landscape in mouse cerebral cortex. (**A**) The number of HC peaks found in both WT and KO cortex (common), or peaks found in both replicates of one genotype but in neither replicate of another (specific). HC peaks of one genotype that were found in only one replicate of another genotype were not shown. (**B** and **C**) Examples of WT-specific (B) or KO-specific (C) m^{6}A peak in 6-week-old male mouse cortex. IGV tracks displaying overlays of normalized and combined read coverage from two biological replicates of m^{6}A-seq. Read clusters from WT IP samples, *FMR1* KO IP samples and corresponding non-IP (input) samples are shown in blue, red and grey, respectively. The legends below KO track show genomic features. Line, intron; thin box, UTR of exon; thick box, coding region of exon; and arrow, direction of reading frame. The lowermost track marks the location of m^{6}A motif [GAC] or its reverse complementary [GTC]. The data ranges were indicated on the right side of each panel. The blue or red bar below WT track indicates WT-specific or KO-specific m^{6}A sites, respectively. Last: last exon or intron in the transcript. See Supplementary Material, Fig. S2F and G for more examples. (**D**) Violin and bar plots depicting the expression levels of genes whose transcripts contained common HC peaks or HC genotype-specific m^{6}A peaks in WT or KO cortex. Lower/middle/upper position in bar plots indicate 25/50/75% quantile, respectively. *, *P*-value < 0.05; ****, *P*-value < 0.0001; *n.s.*, not significant, two-tailed Mann-Whitney *U*-test. (**E** and **F**) GO analyses of genes whose transcripts contained at least one WT-specific (E) or KO-specific (F) m^{6}A peak in 6 week old cortex.

(taking exon–exon junctions and reads' variances among replicates into consideration) and to detect differential methylation (DM) among these m^{6}A sites (*Fmr1* KO versus WT). In total the transcripts of 5963 genes were found to harbor at least one exome-based m^{6}A peak in both WT and KO cortex (Supplementary Material, Table S3). The MeRIP tag enrichment of exome-based m^{6}A peaks within FMRP target transcripts overall showed little bias towards WT or KO cortex (Supplementary Material, Fig. S3A), and only 3 out of 590 m^{6}A-marked FMRP targets contained differentially methylated m^{6}A peaks (KO versus WT, FDR < 0.05; Supplementary Material, Table S3). But on average the expression level of m^{6}A-marked FMRP targets was greatly reduced by *Fmr1* KO (Supplementary Material, Fig. S3B). We postulated that the loss of FMRP could alter transcriptome, so pairwise differential gene expression analysis was performed (KO versus WT). Indeed, a considerable number of differentially expressed genes were identified (Fig. 3A and Supplementary Material, Fig. S3C and Table S2). GO analyses showed that 952 *Fmr1* KO-upregulated genes were mainly enriched for GO terms related to translation and energy (ATP) production, while 1083 *Fmr1* KO-downregulated genes were enriched for biological processes like transcription, intracellular signaling transduction, epigenetic modification and

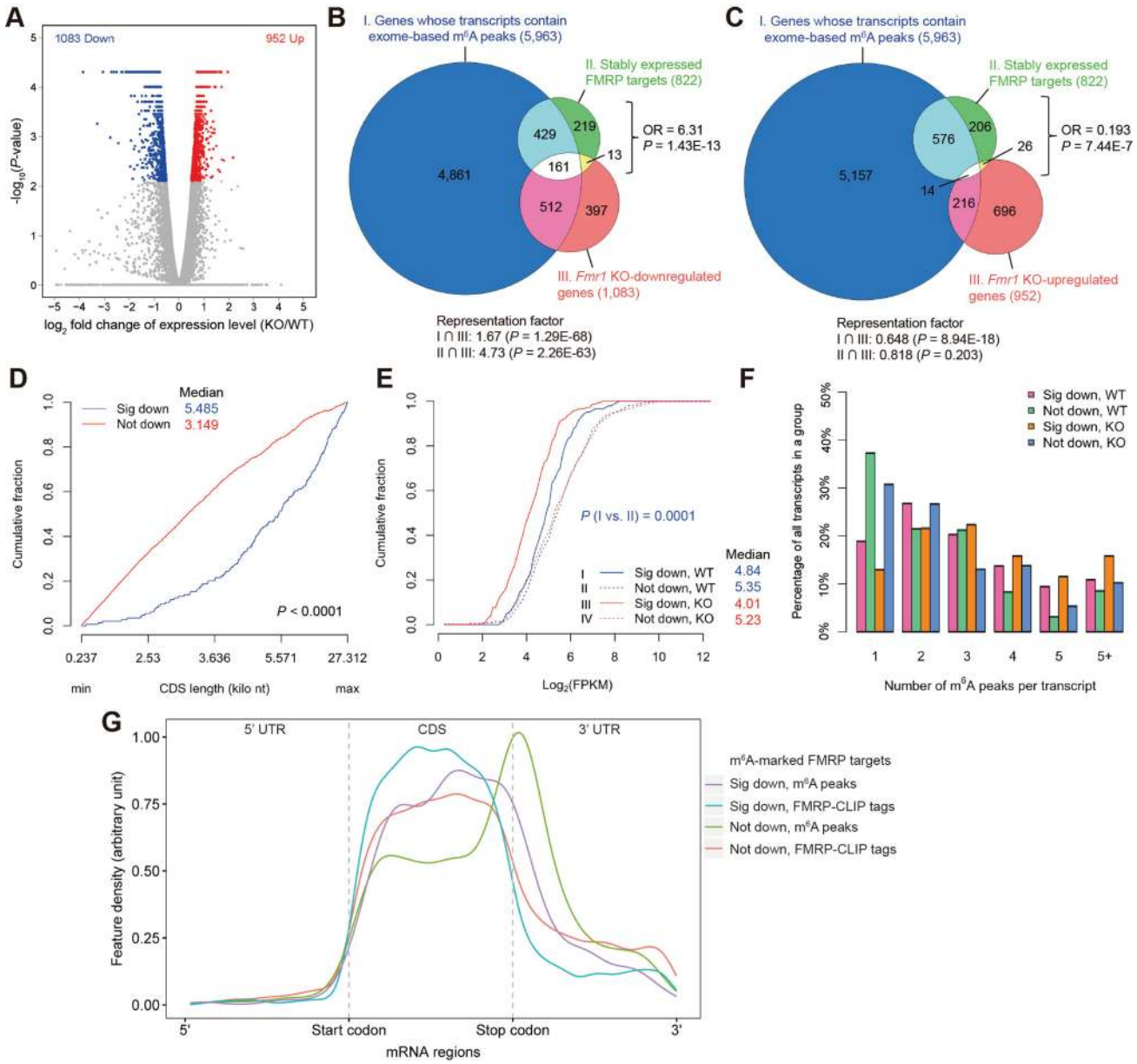

Figure 3. Loss of FMRP leads to downregulation of long m^{6}A-marked FMRP mRNA targets. (**A**) Volcano plot showing transcriptome-wide $\log_2$ fold change in gene expression and corresponding *P*-value. *Fmr1* KO-upregulated and -downregulated genes are highlighted in red and blue, respectively. (**B** and **C**) 3-D Venn diagrams showing the overlaps between stably expressed m^{6}A genes, FMRP targets and *Fmr1* KO downregulated (B) or upregulated (C) genes. Total number of stably expressed genes in WT and *Fmr1* KO cortex combined was 16 003. OR, odds ratio. Fisher's exact test (contingency within II) and Chi-square test (I ∩ III and II ∩ III). (**D** and **E**) Cumulative distribution function plots of m^{6}A-marked FMRP mRNA targets based on either the length of CDS (D) or the level of expression (E). Transcripts were grouped and coded based on indicated bins. If a gene has multiple transcript variants, the longest one in RefSeq was used (D). Sig down, transcripts significantly downregulated in cortex by *Fmr1* KO. WT, in WT cortex; KO, in *Fmr1* KO cortex. nt, nucleotide. Two-tailed Mann–Whitney *U*-test. (**F**) Bar plots showing that among 590 m^{6}A-marked FMRP targets, the 161 *Fmr1* KO-downregulated ones contained more m^{6}A peaks per transcript than the rest 429 in both WT and *Fmr1* KO cortex. (**G**) Metagene plot showing the distribution of m^{6}A peaks and FMRP-CLIP tags across the length of m^{6}A-marked FMRP target mRNAs. 5' UTR, CDS and 3' UTR of Ensembl mRNAs were individually scaled, and the center of exome-based m^{6}A peaks in WT cortex or the center of FMRP-CLIP tags (GSM1098057) was used to calculate the moving average of density. The median widths of exome-based m^{6}A peaks are comparable between the two indicated groups (201 versus 200 nt). If a gene has multiple transcript variants, the longest one in Ensembl was used.

ion transport (Supplementary Material, Fig. S3D and E). Surprisingly, only those downregulated genes, but not the upregulated ones, showed significant overlaps with both FMRP target genes (II ∩ III) and with genes whose transcripts were marked by m^{6}A (I ∩ III) (Fig. 3B and C). More importantly, more than 92% of 174 *Fmr1* KO-downregulated FMRP target mRNAs were marked by m^{6}A with an OR of 6.31, meaning that among stably expressed FMRP targets in KO cortex, m^{6}A-marked ones were significantly downregulated 6.31 times more often than the ones with no m^{6}A (Fig. 3B). Oppositely, if they were marked by m^{6}A, FMRP targets were less likely to be upregulated in KO cortex than in WT cortex (Fig. 3C). To investigate whether these m^{6}A-marked FMRP targets were also downregulated at protein level in *Fmr1* KO cortex, we sampled two genes, *Ntrk3* (neurotrophic receptor tyrosine kinase 3) and *Kcnq2* (potassium voltage-gated channel subfamily Q member 2). *Ntrk3* and *Kcnq2* were downregulated by 61 and

47% at mRNA level, respectively, by *Fmr1* KO (Supplementary Material, Table S2). Western blotting of cortical samples of WT and KO male littermates validated that the proteins encoded by *Ntrk3* and *Kcnq2* were also downregulated in *Fmr1* KO cortex (Supplementary Material, Fig. S3F). So at least for some FMRP targets in brain, the small overall increase in protein synthesis in the absence of functional FMRP (36) was not able to mask the effect of decreased mRNA level.

Next, we scrutinized the 161 genes whose transcripts were m^{6}A-marked, targeted by FMRP and downregulated by *Fmr1* KO in cortex. GO analysis showed that these genes were enriched for specific GO terms (Supplementary Material, Fig. S3G) and pathways (Supplementary Material, Fig. S3H). Moreover, among the 590 FMRP targets containing exome-based m^{6}A peaks, we compared the 161 downregulated in *Fmr1* KO cortex with the 429 not downregulated to determine the differences in various aspects of mRNAs and m^{6}A modification. Interestingly, the 161 mRNAs downregulated by *Fmr1* KO overall are much longer and contain more exons than the 429 mRNAs which were not downregulated (Supplementary Material, Fig. S4A and B). The difference in mRNA length is largely due to the longer CDS in *Fmr1* KO-downregulated FMRP targets (Fig. 3D and Supplementary Material, Fig. S4C and D). Furthermore, even in WT cortex, these downregulated mRNAs on average were expressed at lower level than those not downregulated (Fig. 3E). Also, in either WT or KO cortex, the 161 downregulated mRNAs in general harbored more exome-based m^{6}A peaks than the 429 mRNAs not downregulated (Fig. 3F), but tag enrichment (IP/non-IP ratio within m^{6}A peaks) between these two groups showed no significant difference (Supplementary Material, Fig. S4E). Lastly, we compared the distribution patterns of exome-based m^{6}A peaks across the length of these two groups of mRNAs. Metagene plot revealed that m^{6}A peaks from 161 *Fmr1* KO-downregulated FMRP targets were more enriched in the CDS than m^{6}A peaks from 429 FMRP targets that were not downregulated by *Fmr1* KO. But the distribution patterns of FMRP-CLIP tags (36) in these two groups of mRNAs were similar (predominantly in the CDS) (Fig. 3G). In summary, we discovered that the loss of FMRP in cortex led to significant downregulation of a subset of m^{6}A-marked FMRP target mRNAs sharing characteristics like having long CDS marked by m^{6}A peaks and being moderately expressed. These findings suggested a mechanistic link between the m^{6}A modification on this subset of FMRP targets and the reduced levels of these mRNAs when FMRP was missing.

FMRP binds to m^{6}A sites and is associated with an m^{6}A reader, YTHDF2

The role for m^{6}A in regulating mRNA stability has been well established. YTHDF2, a cytoplasmic m^{6}A reader protein of the YT521-B homology (YTH) domain family, expedites the decay of m^{6}A-marked transcripts by recruiting the CCR4–NOT deadenylase complex (44) and by targeting its cognate mRNAs for degradation in processing bodies (18). Notably, the more m^{6}A/YTHDF2-binding sites one transcript contains, the larger destabilizing effect YTHDF2 will bring to that transcript (18). Since the consensus binding motif of YTHDF2 (18) is almost identical to the m^{6}A motifs found in cortex (Fig. 1B and Supplementary Material, Fig. S2C), and these m^{6}A motifs greatly overlap with FMRP consensus binding motifs (38), we hypothesized that FMRP, as an RNA-binding protein, might bind to the m^{6}A sites in its target mRNAs directly. The first evidence comes from an integrated analysis of our m^{6}A-seq results and previously published matched HITS-CLIP data for FMRP and ELAVL1/HuR/HuA, two selective neuronal RNA binding proteins, in mouse brain (36) (Fig. 4A). FMRP binding is clearly enriched at exome-based m^{6}A sites, consistent with a previous study (39). But ELAVL1 binding is not. About 54% of m^{6}A sites on FMRP target transcripts overlap with FMRP-CLIP tags, while only 28% of m^{6}A sites on ELAVL1 target transcripts overlap with ELAVL1-CLIP tags. Subsequently, the direct binding between FMRP and m^{6}A-marked RNA sequences was tested with an *in vitro* binding assay using purified c-MYC-tagged FMRP and synthetic RNA probes with methylated or unmethylated m^{6}A motifs. The 40 nt long 5'-biotinylated RNA probes were designed based on an m^{6}A peak within the last exon (E14) of *Ntrk3* transcript variant 2 (NM_182809), which was significantly downregulated in *Fmr1* KO cortex (Supplementary Material, Table S2). The positions of m^{6}A modification in the probes were designed by considering the summit of the exome-based m^{6}A peak in cortex (Supplementary Material, Table S3) and the location of m^{6}A consensus motifs within the peak, and by referring to an m^{6}A-CLIP (cross-linking immunoprecipitation) site in whole brain (GSM1828593) (45). Anti-FMRP blotting after streptavidin pull down showed that FMRP could directly bind to the m^{6}A-marked RNA probe. However, FMRP also bounds to the same RNA sequence with no methylation on the two indicated adenosines, and its binding affinities for A and m^{6}A were indistinguishable (Fig. 4B and Supplementary Material, Fig. S5A). Furthermore, to investigate if FMRP binding depends on sequence context instead, we mutated the sequence of the biotinylated RNA probe to remove all known FMRP-binding motifs. Although the m^{6}A modifications were unchanged, the binding affinity of FMRP for the 40 nt long mutant probe has been reduced (Fig. 4B).

We further examined whether FMRP could directly interact with YTHDF2. In a co-immunoprecipitation (co-IP) assay, FLAG-tagged YTHDF2 was transfected into mouse Neuro 2a (N2A) cell line. Anti-FLAG IP followed by anti-FMRP blotting demonstrated that endogenous FMRP interacted with YTHDF2 (Fig. 4C). The interaction between these two RNA-binding proteins was not RNA-dependent since the RNase treatment did not abolish their association (Fig. 4C). Furthermore, EGFP-FLAG-tagged FMRP and FLAG-tagged YTHDF2 were co-transfected into human HEK293T cells for reciprocal IP. Anti-GFP IP followed by anti-FLAG blotting confirmed that FMRP interacts with YTHDF2 in an RNA-independent manner (Fig. 4D). Taken together, these results demonstrate that FMRP could bind to m^{6}A-marked RNA and interact with the m^{6}A reader YTHDF2.

FMRP modulates the stability of its mRNA targets marked by m^{6}A through YTHDF2

Given that FMRP could bind to m^{6}A sites and associate with YTHDF2, we hypothesized that the loss of FMRP could accelerate the degradation of those m^{6}A-marked FMRP targets through YTHDF2. To test this hypothesis, we first investigated if FMRP targets in brain are also bound by FMRP in N2A cells. RNA immunoprecipitation (RIP) was performed for FMRP in N2A cell lysate (Supplementary Material, Fig. S5B), and gene-specific reverse transcription quantitative polymerase chain reaction (RT-qPCR) was used to measure the relative level of transcripts co-immunoprecipitated with FMRP. Six m^{6}A-marked mRNAs (*Ntrk3*; serine/arginine repetitive matrix 2, *Srrm2*; *Kcnq2*; tau tubulin kinase 2, *Ttbk2*; DOT1-like histone lysine methyltransferase, *Dot1l*; and tetratricopeptide repeat, ankyrin repeat and coiled-coil containing 2, *Tanc2*), which are FMRP targets in brain and were among top *Fmr1* KO-

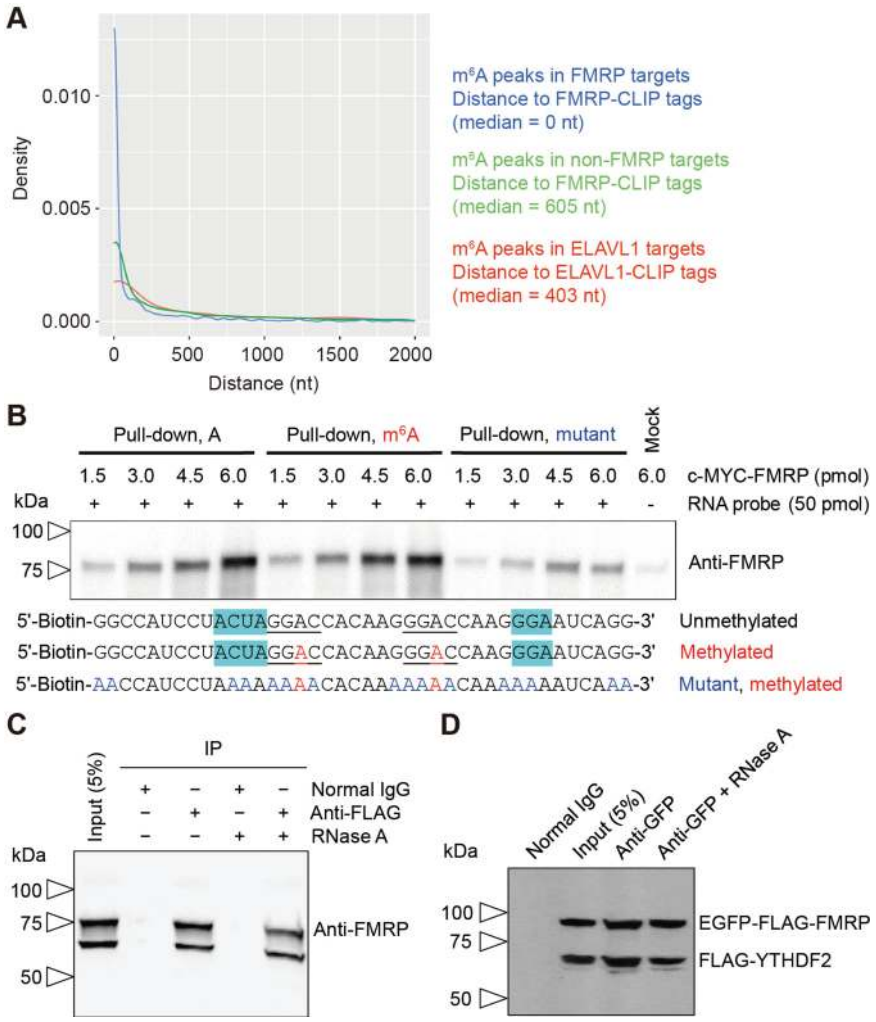

Figure 4. FMRP binds to m^{6}A sites and is associated with YTHDF2. **(A)** Density plot depicting the distances from exome-based m^{6}A peaks to their nearest FMRP- or ELAVL1-CLIP tags in WT mouse brain. In total, 68 178 and 98 832 unique FMRP- and ELAVL1-CLIP tags from the same P13 mouse brain lysate (GSM1098057 and GSM1098059), respectively, were used. In total, 1592 m^{6}A peaks in FMRP target transcripts (blue) were analyzed. The distances from 10 305 m^{6}A peaks in transcripts not targeted by FMRP to their nearest FMRP-CLIP tags (green) and the distances from 340 m^{6}A peaks in ELAVL1 target transcripts to their nearest ELAVL1-CLIP tags (red) are shown as controls for specificity. Median size of FMRP-CLIP tags is 46 bp. If an m^{6}A peak overlaps with any fraction of an FMRP-CLIP tag, the distance between them is considered as 0 bp. **(B)** Western blot showing recombinant FMRP pulled down by 40-nucleotide biotinylated RNA probes. The design of synthetic RNA probes was based on an m^{6}A-marked region within exon 14 of *Ntrk3* mRNA (transcript variant 2, NM_182809). The sequences of the probes are provided at the bottom, with two m^{6}A motifs underlined and the other two FMRP binding sequences highlighted in cyan. Red, m^{6}A; blue, mutated bases. **(C)** Western blotting showing endogenous FMRP co-immunoprecipitated with FLAG-tagged YTHDF2 by anti-FLAG antibodies in N2A cells. The migrations of protein mass standards are indicated on the left. Input, non-IP sample. **(D)** Anti-FLAG western blotting showing that FLAG-tagged YTHDF2 were co-immunoprecipitated with EGFP-FLAG-tagged FMRP by ant-GFP antibodies in 293T cells. Blots in (B–D) are representative images of two (B) or three (C and D) biological replicates and have been cropped to improve the clarity and conciseness of the presentation.

downregulated mRNAs in cortex, were found to be enriched by RIP and associated with FMRP to a similar level as two validated FMRP targets (microtubule associated protein 1B, *Map1b*; and calcium/calmodulin-dependent protein kinase II α, *Camk2a*) (29), indicating that these six mRNAs are also targets of FMRP in N2A cells (Supplementary Material, Fig. S5C and D). We then applied RNA interference to N2A cells. Knockdown (KD) *Fmr1* using small interfering RNA (siRNA) downregulated the level of the six m^{6}A-marked FMRP target mRNAs (*Ntrk3*, *Srrm2*, *Kcnq2*, *Ttbk2*, *Dot1l* and *Tanc2*) and two FMRP target mRNAs without m^{6}A peak (GRAM domain containing 1B, *Gramd1b*; and ankyrin repeat domain 52, *Ankrd52*) in N2A cells, recapitulating the finding in 6 week old cerebral cortex (Fig. 5A and Supplementary Material, Fig. S5E).

Next, we measured the decay rates of mRNAs in N2A cells transfected with siRNA(s). Global transcription in N2A cells was blocked by actinomycin D treatment. The mRNA level in relation to a spike-in mRNA was measured at different time points after transcription inhibition, and the first-order decay rate was determined by linear regression. METTL14 plays a critical role for substrate recognition in the multi-component m^{6}A 'writer' complex (3,4). KD or conditional KO of *METTL14*/*Mettl14* greatly reduces m^{6}A levels (2,27,46). As expected, *Mettl14* KD in N2A cells significantly reduced the decay rates of the six m^{6}A-marked FMRP targets compared with the scrambled control, but the decay rates of *Rpl15* (ribosomal protein L15) and *Hprt* (hypoxanthine phosphoribosyltransferase) mRNAs, which lack m^{6}A, were unchanged, suggesting that the degradation of those m^{6}A-marked FMRP targets was regulated by m^{6}A (Fig. 5B and C and Supplementary Material, Fig. S5F and G and Fig. S6A–F). Furthermore, on average about 80% KD of *Fmr1* significantly

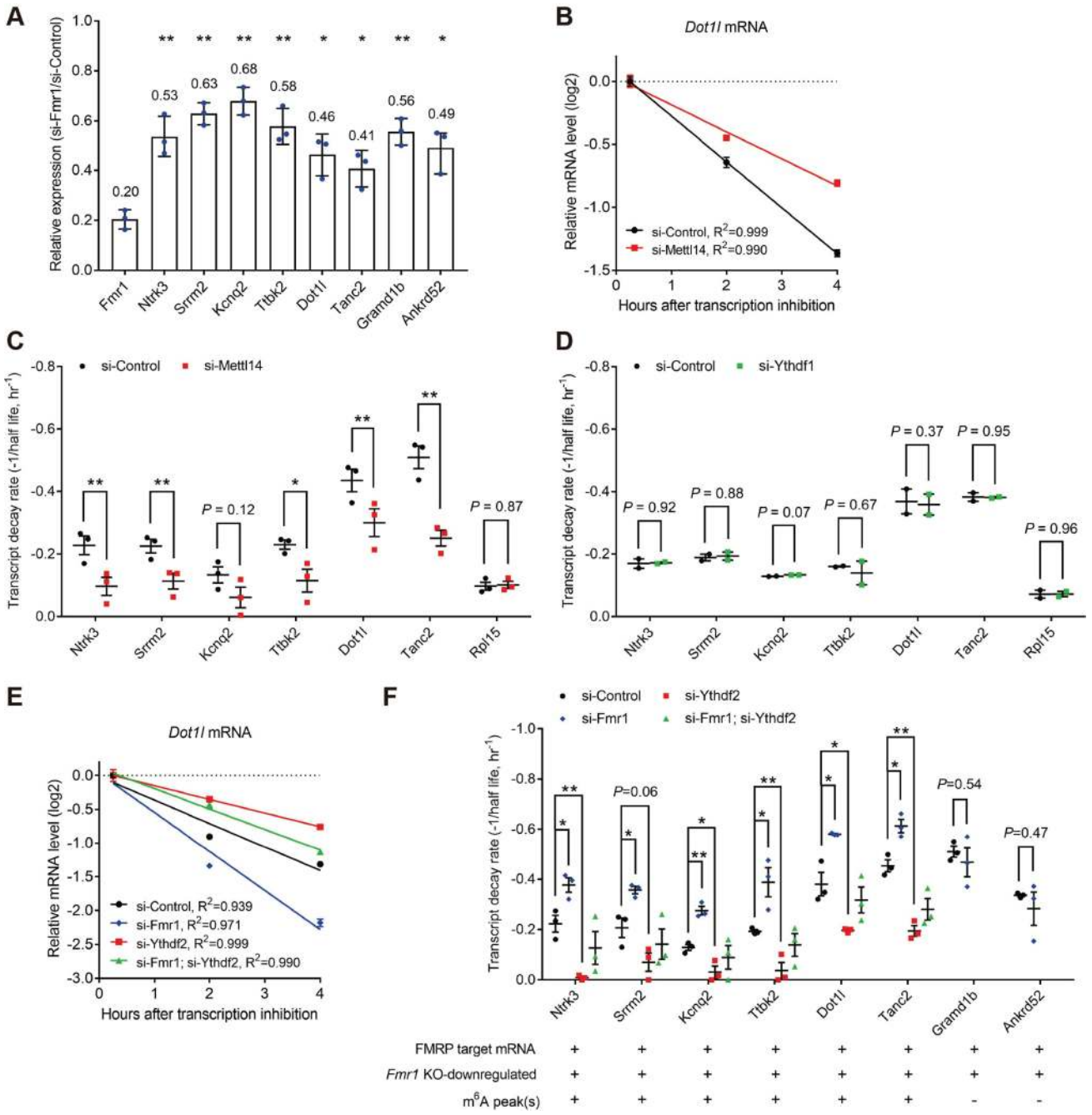

Figure 5. FMRP regulates the stability of its m^{6}A-marked mRNA targets. (**A**) Gene-specific RT-qPCR results showing relative mRNA levels in N2A cells with *Fmr1* KD (si-*Fmr1*). *Rpl15* mRNA served as an internal control. Individual data points and mean ± SD of three biological replicates (each with three technique replicates) are shown. *, *P*-value < 0.05; **, *P*-value < 0.01, two-tailed one-sample *t*-test. (**B** and **E**) Representative plots for calculating the decay rates of transcripts in N2A cells under si-control or si-*Mettl14* (B) and under si-control, si-*Fmr1*, si-*Ythdf2* or si-*Fmr1* plus si-*Ythdf2* (double KD) (E). Transcription was inhibited by Actinomycin D treatment. *Dot1l* mRNA abundance was normalized to a spike-in control (luciferase mRNA). Mean ± SD of three technique replicates in one of the three biological replicates are shown. Decay rate equals to the slope of the linear regression line. See Supplementary Material, Fig. S6 for more examples of FMRP targets marked by m^{6}A and negative controls. (**C**, **D** and **F**) Transcript decay rates in N2A cells under si-control or si-*Mettl14* (C), under si-control or si-*Ythdf1* (D) and under si-control, si-*Fmr1*, si-*Ythdf2* or si-*Fmr1* plus si-*Ythdf2* (F). Actinomycin D was used to block global transcription. Individual data points and mean ± SEM of two to three biological replicates (each with three technique replicates) are shown. *, *P*-value < 0.05; **, *P*-value < 0.01, two-tailed *t*-test.

increased the decay rates of the six *Fmr1* KO-downregulated FMRP targets marked by m^{6}A, in comparison to the scrambled control (Fig. 5E and F and Supplementary Material, Fig. S6G–J), indicating that expedited degradation played an evident role in reducing the steady-state level of these mRNAs during *Fmr1* downregulation. However, *Fmr1* KD did not accelerate the decay of the two *Fmr1* KO-downregulated FMRP targets with no m^{6}A site (*Gramd1b* and *Ankrd52*) (Fig. 5F and Supplementary Material, Fig. S6K), suggesting that the stabilizing effect of FMRP for its targets was mediated by m^{6}A. It is worth noting that we have examined three additional *Fmr1* KO-downregulated FMRP target mRNAs without m^{6}A peak (mindbomb E3 ubiquitin protein

ligase 1, *Mib1*; chromodomain helicase DNA binding protein 3, *Chd3*; and FCH domain only 1, *Fcho1*), but their decay rates could not be determined because none of them showed appreciable amount of degradation at 6 h after actinomycin D treatment.

Lastly, we investigated if the degradation of these m^{6}A-marked FMRP targets was mediated by YTHDF2. On average about three-quarter KD of *Ythdf2* reduced the decay rates of the six m^{6}A-marked FMRP targets by at least 50% in comparison to the scrambled control (Fig. 5E and F and Supplementary Material, Fig. S5J, S5K and S6G–J). On the contrary, downregulation of YTHDF1, another cytoplasmic m^{6}A reader protein and a homolog of YTHDF2, did not alter the decay rates of those mRNAs (Fig. 5D and Supplementary Material, Fig. S5H and S5I). Furthermore, *Ythdf2* KD abolished the expedited degradation of these m^{6}A-marked FMRP targets induced by *Fmr1* KD (Fig. 5E and F and Supplementary Material, Fig. S6G–J). As a negative control, the stability of *Hprt* mRNA, which was neither an FMRP target (36) nor an YTHDF2 target (18), was not affected by si-Fmr1 and/or si-Ythdf2 (Supplementary Material, Fig. S6L). Taken together, these results suggested that the degradation of the *Fmr1* KO-downregulated and m^{6}A-marked FMRP targets was mainly through YTHDF2, and FMRP could stabilize this subset of its targets.

Discussion

FXS is the most common inherited form of intellectual disability and a leading genetic cause of ASD. FXS is caused by the loss of functional FMRP (29–32). FMRP is a selective RNA-binding protein associated with polyribosome (33–35). It has been well established that FMRP could regulate the translation of its mRNA targets. Here we show that in brain a significant portion of FMRP mRNA targets are marked by m^{6}A, the most prevalent internal RNA modification of mammalian mRNAs. Biochemically FMRP could bind to the m^{6}A sites of its mRNA targets and interact with YTHDF2, an m^{6}A reader, in an RNA-independent manner. Mechanistically we demonstrated that FMRP could maintain the stability of its mRNA targets while YTHDF2 promotes the degradation of these mRNAs. These data together provide the first link between FMRP and mRNA stability regulated through m^{6}A, revealing an additional layer of gene regulation mediated by FMRP.

The observation that the consensus sequence for m^{6}A methylation (RGACH) largely overlaps with FMRP-bound YGGA and GAC motifs raised the possibility that FMRP could directly bind to the m^{6}A sites in its targets. It has been shown that the YTH domain of m^{6}A reader proteins, YTHDF1 and YTHDF2, exhibits 16- to 20-fold higher binding affinity for an m^{6}A-marked RNA probe than for an unmethylated one with the same sequence (18). FMRP is a context-dependent RNA-binding protein (47) and three categories of RNA binding motifs are present in FMRP: two Agenet motifs, three KH (heterogeneous nuclear RNP K homology) motifs and an RGG (Arg-Gly-Gly) box (48). However, FMRP does not carry YTH domain. Using RNA-binding assay, we found that FMRP did not display preferentially binding to an m^{6}A-marked RNA probe (based on an *in vivo* m^{6}A site) over an unmethylated one with the same sequence, albeit a recent study reported that FMRP displayed about 2-fold preference for a 20 nt m^{6}A-marked RNA probe with sequence $(GGACU)_4$ over an unmethylated one (39). Nevertheless, it is still possible that some 'm^{6}A-switches' (20,21) *in vivo* can alter local RNA structures (like stem-loops or G-quartets) to modulate the accessibility of FMRP binding sites. In addition, there is overt difference in the distribution of FMRP binding sites and m^{6}A sites across the length of FMRP target mRNAs. It has been shown that FMRP predominantly binds the CDS with no specific position relative to the start and stop codons (Fig. 3G) (36,38), while m^{6}A sites are abundant not only in the CDS but also in the 3' UTR and are highly enriched near the stop codon (22). Moreover, for individual FMRP target mRNAs, an even distribution of FMRP binding along the CDS has been observed (36), but on average there are only ~3–5 m^{6}A per mRNA which most likely will restrict m^{6}A readers to very specific binding sites (49). Taken together, this evidence supports that FMRP can bind to m^{6}A-marked mRNA, but unlike m^{6}A reader proteins, its binding most likely depends on sequence context rather than methylation status.

We found that the loss of FMRP could alter m^{6}A epitranscriptome in cortex, leading to both gain and loss of m^{6}A peaks in transcripts enriched for transcriptional and synaptic functions. Surprisingly, a significant portion of those downregulated mRNAs, but not the upregulated ones, are FMRP targets and almost all of them are marked by m^{6}A.

We also noticed that the m^{6}A peaks from *Fmr1* KO-downregulated FMRP targets were more likely to locate in the CDS than the m^{6}A peaks from FMRP targets that were not downregulated by *Fmr1* KO. Given the fact that FMRP binding sites located predominantly in the CDS, this finding implies higher level of interplay between FMRP and m^{6}A reader in regulating those *Fmr1* KO-downregulated FMRP targets. Using mouse neuronal cells, we demonstrated that FMRP maintains the stability of its long mRNA targets marked by m^{6}A, while m^{6}A marks and YTHDF2 promotes their degradation, suggesting a competition between FMRP and YTHDF2 for binding to the m^{6}A sites on these mRNAs. In agreement with the literature (13), YTHDF1 did not seem to regulate the stability of those mRNAs. In addition, we showed that FMRP interacts with YTHDF2 in an RNA-independent manner. Thus, it is possible that FMRP not only competes with m^{6}A readers for binding to overlapped sites in certain neural mRNAs, but also modulates m^{6}A-mediated regulation of mRNA homeostasis directly via interacting with m^{6}A reader proteins (Supplementary Material, Fig. S7).

FMRP is known to repress the translation of a set of synaptic plasticity-related mRNAs by causing translating ribosomes to stall and accumulate on the mRNA (36). This repression can be relieved by dephosphorylation and ubiquitination of FMRP, presumably in response to synaptic activation, resulting in rapid protein production with precise timing (50,51). Recently, a competition between FMRP and YTHDF1 for binding to m^{6}A sites has been speculated (39). If confirmed, this competition will suggest an antagonism between FMRP and m^{6}A pathway in the control of translational efficiency of mRNAs. In addition, a role for FMRP in the control of mRNA stability has been proposed. For example, FMRP stabilizes one of its targets, *Dlg4* (PSD-95) mRNA, in hippocampus but not in cortex (52). FMRP has also been shown to destabilize *Nxf1* mRNA in N2A cells (53). However, neither of these two mRNAs contain exome-based m^{6}A peak in cortex (Supplementary Material, Table s3). Herein, we showed that FMRP stabilizes m^{6}A-marked neural mRNAs containing long CDS most likely by impeding m^{6}A/YTHDF2-mediated degradation, and the proteins encoded by these mRNAs are significantly involved in synapses, signaling pathways and long-term potentiation. This novel mechanism, together with m^{6}A-regulated local translation (54) and potential interplay among FMRP and other m^{6}A readers in YTH domain family, could further ensure timely local protein synthesis from existing FMRP target mRNAs upon the stimulation.

Our m^{6}A profiling in adult mouse cerebral cortex revealed more than 47% of stably expressed cortical genes whose

transcripts contain high-confidence m^{6}A sites, corroborating that m^{6}A is a widespread epitranscriptomic modification in cortex. FXS not only represents the most common inherited form of intellectual disability but also is the most common monogenic cause of ASD (31). FXS patients often display autistic behaviors, with about 70% of them meeting diagnostic criteria for ASD (55). A significant overlap of FMRP targets and 117 autism-related genes has been reported (36). To date, among 870 mouse homologs of autism candidate genes in the SFARI database, 172 (20%) of them are regulated by FMRP (a significant overlap, *P*-value = 1.9E-97, Chi-square test) with 84% (144 genes) marked by m^{6}A in this study (Supplementary Material, Tables S1 and S2). Notably, within 144 ASD-related and m^{6}A-marked FMRP targets, one-third (48 genes) were significantly downregulated by *Fmr1* KO, in contrast to only 2% (3 genes) upregulated (Supplementary Material, Tables S2). This finding supports that FMRP-mediated regulation on mRNA stability may be relevant to the autistic features in FXS. Since a stringent set of 842 FMRP target transcripts and stringent m^{6}A peak calling algorithms were used in our study, the true number of mRNAs whose decay is modulated by both FMRP and m^{6}A pathway may be underestimated.

In summary, we show that m^{6}A is a widespread epitranscriptomic modification in mammalian cortex, and FMRP modulates the stability of its mRNA targets in concert with m^{6}A pathway. Also, we revealed dysregulated transcriptome and epitranscriptome in the absence of FMRP, providing a resource for studying molecular pathogenesis of FXS. The work presented here represents the first link between FMRP and m^{6}A-regulated neural mRNA stability, which could contribute to the pathogenesis of FXS.

Materials and Methods

Animals

Control WT mice (C57BL/6J, Jackson Laboratory, Bar Harbor, ME, stock # 000664) and *Fmr1* KO mice (generated on the same background, C57BL/6J *Fmr1*^{tm1Cgr}, available from Jackson Laboratory, stock # 003025) were housed, maintained and euthanized according to the Emory University Institutional Animal Care and Use Committee guidelines. *Fmr1* KO males and their WT male littermates were obtained by crossing WT males with *Fmr1*^{tm1Cgr} heterozygous females. Genotyping was determined by standard PCR using a mutant reverse primer (5′-TTCGACCACCAAGCGAAACATC-3′) or a WT reverse primer (5′-TCCAGCTTGATCTTATGGAAAG-3′), with a common forward primer (5′-GTGATAGAATATGCAGCATGTG-3′). Hemizygous mutant males and WT males generate ∼750 bp and ∼120 bp PCR products, respectively.

m^{6}A-seq

Six week old male mice were euthanized using CO_2. Total cellular RNA was isolated from fresh mouse cortex using TRIzol Reagent (Thermo Fisher, Waltham, MA) and Phase Lock Gel, Heavy (QuantaBio, Beverly, MA) per manufacturers' protocols. For each biological replicate, total RNA samples isolated from the cortex of six 6 week old male mice were pooled. mRNA isolation and clean up, m^{6}A-RIP, RNA-seq library preparation and next-generation sequencing were performed as previously described (28).

Mammalian cell culture and siRNA transfection

N2A mouse neuroblastoma cells (ATCC, Manassas, VA, CCL-131) were grown in Minimum Essential Medium (Corning, Corning, NY, 10-009-CV), supplemented with 10% (vol/vol) fetal bovine serum (FBS) (Atlanta Biologicals, Flowery Branch, GA) and 100 units/mL penicillin plus 100 µg/mL streptomycin (Thermo Fisher). 293T human embryonic kidney epithelial cells expressing SV40 T antigen (ATCC, CRL-3216) were grown in Dulbecco's Modified Eagle Medium (DMEM) (Thermo Fisher, 11995065), supplemented with 10% FBS, 2 mM L-glutamine (Thermo Fisher) and 100 units/mL penicillin plus 100 µg/mL streptomycin. The genotypes of transformed cell lines were verified by ATCC, and only cells with low passage number (< 20) were used. All cells were maintained in a humidified incubator at 37°C in an atmosphere of 5% CO_2. Dharmacon ON-TARGETplus SMARTpool mouse *Fmr1* siRNA (L-045448-00), mouse *Ythdf1* siRNA (L-050937-01) and mouse *Ythdf2* siRNA (L-058271-01) were used to downregulate *Fmr1*, *Ythdf1* and *Ythdf2* in N2A cells, respectively. Qiagen negative control siRNA (1027310) was used as the scrambled control. For RNA interference, 25 nM siRNA oligos were transfected into N2A cells (for example, 0.5 million cells plated about 16 h ago in 2 mL of growth medium) using Lipofectamine RNAiMAX (Thermo Fisher) per manufacturer's protocol. One day later, transfected cells were split (1:3) with fresh growth medium.

Western blotting

Six week old male mouse cortex was homogenized and lysed in RIPA buffer (25 mM Tris•HCl pH 7.6, 150 mM NaCl, 1% NP-40, 1% sodium deoxycholate and 0.1% SDS) supplemented with cOmplete Protease Inhibitor Cocktail (Roche, Basel, Switzerland). The protein concentration of cleared lysate was determined by Pierce BCA Protein Assay Kit (Thermo Fisher) and a Synergy H4 Multi-Detection Microplate Reader (BioTek, Winooski, VT) per manufacturer's instructions. For RNAi experiments, cell lysate was prepared at 72 h after transfection. Lysate samples were denatured in 2× Laemmli Sample Buffer (Bio-Rad, Hercules, CA) at 95°C, separated by SDS–polyacrylamide gel electrophoresis (PAGE) on Mini-PROTEAN TGX Precast Mini Gels (Bio-Rad), transferred onto 0.2 µm PVDF membrane by Trans-Blot Turbo Blotting System and Mini Transfer Pack (Bio-Rad) and probed with primary antibodies against FMRP (1:2000, rabbit pAb, abcam, Cambridge, United Kingdom, ab17722), TrkC (1:1000, rabbit mAb (C44H5), Cell Signaling Technology, Danvers, MA, 3376), Kv7.2 (1:500, rabbit mAb (D9L5S), Cell Signaling Technology, 14752), METTL14 (1:2000, rabbit pAb, Sigma-Aldrich, St. Louis, MO, HPA038002), YTHDF1 (1:1000, rabbit pAb, proteintech, Chicago, IL, 17479-1-AP), YTHDF2 (1:1000, rabbit pAb, abcam, ab170118), FLAG tag (1:2000, mouse mAb (M2), Sigma-Aldrich, F3165 or rabbit pAb, Sigma-Aldrich, SAB1306078) and GAPDH (1:10 000, mouse mAb (6C5), Santa Cruz Biotechnology, Dallas, TX, sc-32233) in 5% of nonfat dry milk in 1× TBST (0.1% Tween 20) at 4°C overnight. Primary antibodies were labeled by HRP-linked secondary antibodies (1:4000, Cell Signaling Technology). In western blotting analyses of anti-FMRP RIP, the primary anti-FMRP rabbit pAb was labeled by TrueBlot Anti-Rabbit IgG HRP (1:1000, Rockland Immunochemicals, Limerick, PA) to avoid the detection of denatured anti-FMRP antibody used for IP. The enhanced chemiluminescent signals were detected using HyGLO Quick Spray Chemiluminescent HRP Antibody Detection Reagent (Thomas Scientific, Swedesboro, NJ) and were captured by either ChemiDoc Touch Imaging System (Bio-Rad) or Hyblot CL Autoradiography Film (Denville Scientific). Densitometric quantification of western blotting images was performed using ImageJ/Fiji (56). No pixel used for quantification was overexposed.

Quantitative RT-PCR

Total cellular RNA was purified from N2A cells (72 h after transfection) using TRIzol Reagent and Direct-zol RNA MiniPrep Kit (Zymo Research, Irvine, CA) per manufacturers' protocols. RNA concentration was determined by a NanoDrop 2000 Spectrophotometer (Thermo Fisher), and 1 μg of total RNA was used to synthesize first-strand cDNA. SuperScript III First-Strand Synthesis System for RT-PCR (Thermo Fisher) and random hexamer priming were used. SYBR Green qPCR was performed as previously described (57). TaqMan gene expression assay was used for *Neat1*: 1 μL of sequence-specific TaqMan gene expression primers (20×; Thermo Fisher, Mm01720914_g1), 1 μL of reverse transcription product, 10 μL of TaqMan Universal PCR Master Mix II No UNG (2×; Thermo Fisher) and 8 μL of nuclease-free water. All qPCR reactions were performed in triplicates, and the results were analyzed using the $\Delta\Delta C_T$ method. The internal control for siRNA-transfected N2A cells was *Rpl15*. All SYBR Green qPCR primers were designed to span exon–exon junctions (see Supplementary Material, Table S4 for their sequences).

RNA decay

N2A cells transfected with siRNA(s) were re-plated into 12-well plates at 24 h after transfection and were cultured to ~80% confluence at 72 h after transfection. 5 μm of actinomycin D (Sigma-Aldrich, A9415) was added to inhibit transcription. At 15 min, 2 or 4 h after actinomycin D treatment, cells were washed once with PBS and then lysed in 0.35 mL of Buffer RLT (Qiagen, Hilden, Germany) supplemented with 1% β-mercaptoethanol. Cell lysate was passed through a QIAshredder spin column (Qiagen), and 10 μL of homogenized cell lysate was taken for the quantitation of DNA content using Quant-iT PicoGreen dsDNA Kit (Thermo Fisher) and a Synergy H4 Multi-Detection Microplate Reader (BioTek) per manufacturer's instructions. Before RNA purification, 0.5 ng of luciferase control RNA (Promega, Madison, WI) per 1 μg of DNA content was added to each sample. Total cellular RNA was extracted using RNeasy Micro Kit (Qiagen), and RT-qPCR was performed. For each transcript, ΔC_T was calculated by subtracting the average of C_T numbers of the spike-in luciferase control RNA from the C_T number of the transcript in each sample. And then $\Delta\Delta C_T$ for each sample was calculated by subtracting the average of ΔC_T for the total RNA isolated at 15 min after actinomycin D treatment. The $\log_2$ relative levels of the transcript at the three time points (15 min, 2 and 4 h) were plotted against time, and a linear regression was used to determine the slope, which is the decay rate (k).

co-IP

Human full-length FMR1 tagged with EGFP and FLAG at the *N* terminus in the FUGW plasmid (58) and pcDNA 3.0 with *N*-FLAG-tagged human YTHDF2 (18) were prepared with ZymoPURE Plasmid Maxiprep Kit (Zymo Research). For co-IP experiments, N2A cells (in a 10 cm culture dish) were transfected with 20 μg of *N*-Flag-YTHDF2 plasmid, and 293T cells (in a 10 cm culture dish) were co-transfected with 20 μg of EGFP-FLAG-FMR1 plasmid and 20 μg of *N*-FLAG-YTHDF2 plasmid, using Lipofectamine 3000 (Thermo Fisher) per manufacturer's protocol. At 48 h after transfection, cells were lysed using 1 mL of co-IP Lysis Buffer (50 mM Tris•HCl pH 7.5, 300 mM NaCl, 30 mM EDTA and 0.5% Triton X-100) supplemented with protease inhibitor cocktail at 4°C with rotation for 30 min. Cell lysates were cleared by centrifugation at 20 000× *g* at 4°C for 10 min and were incubated with or without RNase A (Sigma-Aldrich, R6148) and with either 10 μg of anti-GFP rabbit polyclonal antibody (abcam, ab290)/anti-FLAG mouse monoclonal antibody (Sigma-Aldrich, F3165) or 10 μg of normal rabbit/mouse IgG (as a control; Millipore, Burlington, MA) at 4°C with rotation overnight. The immunocomplex was captured by 0.9 mg of Dynabeads Protein G (Thermo Fisher) and was washed three times with co-IP Lysis Buffer. Proteins bound to the beads were eluted by 2× Laemmli Sample Buffer for SDS-PAGE followed by western blotting with anti-FLAG mouse monoclonal antibody (Sigma-Aldrich, F3165).

Pull-down assay

5'-Biotinylated RNA probes were custom synthesized by Integrated DNA Technologies (Coralville, IA) and were purified by RNase-free HPLC. 30 μL of Dynabeads M-280 Streptavidin (Thermo Fisher) was washed three times with 1 mL of immobilization buffer (10 mM Tris•HCl pH 7.5, 1 M NaCl, 1 mM EDTA and 0.01% Tween-20). 10 μm of RNA probes were denatured at 68°C for 6 min and then immediately chilled on ice. 50 pmol of denatured RNA probes were immobilized to 30 μL of washed Dynabeads M-280 Streptavidin in 0.2 mL of immobilization buffer at room temperature for 15 min with rotation. After washing beads twice with 1 mL of binding/washing buffer, 0.5 mg of bovine serum albumin (Sigma-Aldrich) in 0.2 mL of binding/washing buffer (20 mM HEPES pH 7.9, 150 mM NaCl, 2 mM $MgCl_2$ and 0.2% NP-40) supplemented with 1 U/μL of SUPERase•In RNase Inhibitor (Thermo Fisher) was added to the beads. After incubation at 4°C for 1 h with rotation, beads were washed twice with 1 mL of binding/washing buffer and then 0.2 mL of binding/washing buffer supplemented with 1 U/μL of SUPERase•In RNase Inhibitor and indicated amounts of *C*-terminal MYC/FLAG-tagged FMRP recombinant protein (OriGene, Rockville, MD) were added to the beads. In no probe control (mock), 0.2 mL of binding/washing buffer with RNase inhibitor and 6 pmol of recombinant FMRP were added. After binding at 4°C for 1 h with rotation, beads were washed six times with 1 mL of binding/washing buffer (5 min for each wash) and the bound FMRP was eluted by 2× Laemmli Sample Buffer for SDS-PAGE followed by western blotting.

RIP

RIP procedure was adapted from a previous report (59). Two days after plating 1.7 million cells per 10 cm dish, N2A cells in two 10 cm dishes were washed twice with ice-cold PBS, collected by cell scraper into ice-cold PBS and pelleted by centrifuge at 500 g, 4°C for 5 min. The fresh cell pellet was re-suspended with 2 mL of RIP lysis buffer (300 mM NaCl, 50 mM Tris•HCl pH 7.4, 30 mM EDTA and 0.5% Triton X-100) supplemented with protease inhibitor cocktail and 200 U/ml RNaseOUT Recombinant Ribonuclease Inhibitor (Thermo Fisher) and incubated on ice for 10 min. The cell lysate was passed through a small needle (e.g. 26G) several times and centrifuged at 20 000 g, 4°C for 15 min. 80 μL of supernatant was saved as input (10%) for RNA extraction, and another 80 μL of supernatant was set aside for protein analysis. 50 μl of Dynabeads Protein G (Thermo Fisher) was washed twice with 0.7 mL of RIP lysis buffer and re-suspended with 150 μL of RIP lysis buffer. 10 μg of rabbit anti-FMRP polyclonal antibody (abcam, ab17722) or 10 μg of normal rabbit IgG (as a control; Cell Signaling Technology) was added to

the re-suspended magnetic beads, and the mixture was rotated continuously at room temperature for 30 min. After incubation, beads-antibody complex was washed four times with 0.7 mL of RIP lysis buffer, mixed with 0.8 mL of cleared cell lysate and then rotated continuously at 4°C for 3 h. The tubes were centrifuged briefly and placed on a magnetic separator. 80 μL of supernatant was set aside as flow-through (10%) for protein analysis; the beads were collected, washed five times with 0.7 mL of RIP lysis buffer at 4°C and re-suspended with 0.5 mL of RIP lysis buffer. 50 μL of mixture was saved as IP (10%) for protein analysis. The rest of beads (90%) were transferred into a new tube, collected and re-suspended with 150 μL of proteinase K digestion solution [125 μL of NT2 buffer (150 mM NaCl, 50 mM Tris•HCl pH 7.4, 1 mM $MgCl_2$ and 0.05% NP40), 15 μL of 10% SDS and 10 μL of proteinase K (20 mg/ml; Thermo Scientific)]. In parallel, 25 μL of nuclease-free water, 15 μL of 10% SDS and 10 μL of proteinase K were added to the input sample thawed on ice. Proteinase K digestion was carried out at 55°C for 30 min with constant shaking in a thermomixer (1200 rpm). After the digestion, the tubes were centrifuged briefly and placed on a magnetic separator. The supernatant was transferred into a 2 ml tube of Phase Lock Gel Heavy. 250 μL of NT2 buffer was added to the tube, followed by 400 μL of phenol:chloroform:isoamyl alcohol (25:24:1, pH 6.5; Sigma-Aldrich). Tubes were vortexed for 10 s and centrifuged at 15 000 g, 4°C for 10 min. 400 μL of the aqueous phase was transferred into a new tube. RNA was recovered from the aqueous phase by overnight ethanol precipitation with Pellet Paint Co-Precipitant (Millipore) per manufacturer's instructions. Purified input and immunoprecipitated RNA were used in RT-qPCR. In addition, input, flow-through and IP samples were analyzed by SDS-PAGE and western blotting.

Bioinformatics analyses

High-throughput sequencing data in this study are summarized in (Supplementary Material, Table S5). Genome-based m^6A peaks were identified and annotated as previously described (28), except updated versions of Bowtie (v2.2.4) (60) and Homer (v4.7.2) (61) software were used. When the distance between two peak centers is within 100 bp (about the average size of RNA fragments used in m^6A-IP), the two peaks are considered as overlapping (Supplementary Material, Fig. S1C). Integrative Genomics Viewer (IGV) (62,63) was used for creating tiled data files (.tdf) from BAM files (.bam). Genome-wide coverage data were scaled by 1 000 000/total read count and visualized in IGV. DREME (v4.12.0) (64) was used to discover enriched motifs with top 1000 scored HC peaks. Shuffled input sequences were used as control sequences, and only given strand was searched. CentriMo (v4.12.0) (65) was used to search centrally enriched motifs in all HC peaks. Only given strand was searched, and weighted moving average with a 30 nt window was used to smooth plots. Exome-based m^6A peaks (fold enrichment ≥ 2) and DM (FDR ≤ 0.05) in m^6A-seq data of WT and *Fmr1* KO cortex were identified and annotated by R using MeTPeak (v1.1) (42) and MeTDiff (v1.1.0) (43) packages from RNA-seq reads aligned to mouse genome (build mm9) by Tophat v2.0.13 (66). DM sites are defined as the ones with FDR ≤ 0.05 and fold enrichment of the peaks on the hypermethylated side being consistently larger than 2. The FPKM values for gene expression were calculated by Cufflinks (v2.2.1) (67) using UCSC annotation mm9. Stably expressed genes were defined as FPKM ≥ 0.2. Differentially expressed genes were identified by Cuffdiff (v2.2.1) (68) using UCSC mm9 and defined as q-value ≤ 0.05. R was used for statistical processing and visualizing data. MetaPlotR (69), a Perl/R pipeline was used to create the metagene plot. BEDTools closestBED (70) was used to calculate the distance between an exome-based m^6A peak and the nearest FMRP- or ELAVL1-CLIP tag. GSM1098057 in the dataset GSE45148 was chosen for FMRP-CLIP, because it contains significantly more tags obtained by Illumina sequencing (36). GSM1098059 is from the matched ELAVL1-CLIP experiment (36). The list of ELAVL1 targets in mouse brain was obtained from the CLIPdb (71) using Piranha peak caller (v1.2.0) (72). GO analysis was performed by the Database for Annotation, Visualization and Integrated Discovery v6.8 (73). GO mapping of biological process was directly annotated by the source database. No parent terms were shown. Significantly enriched GO terms were defined as FDR (Benjamini–Hochberg) ≤ 0.05. Pathway analysis was performed by the WEB-based Gene SeT AnaLysis Toolkit (WebGestalt) (74) update 2017 with KEGG data source (release 1 October 2016). Significantly enriched pathways were defined as adjusted *P*-value ≤ 0.05. Other bioinformatics analyses were performed in the R computational environment.

Statistical analyses

Investigators were not blinded to *in vitro* experiments. The differences between two groups were determined with at least three replicates, and equal variances were assumed. Details of statistical analyses are included in figure legends. An alpha level of 0.05 was used for significance. Two-tailed *t*-test, Mann–Whitney *U*-test and Wilcoxon matched-pairs signed rank test, and linear regression were performed in Prism 7 (GraphPad Software). Fisher's exact test, Chi-square test and Pearson's *r* test were performed in R. *P*-values are indicated in figures and figure legends. When calculating statistical significance of overlapping genes sets, all genes stably expressed in our RNA-seq dataset were used as the total set of genes, and the numbers are indicated in figure legend.

Data and code availability

The m^6A-seq data reported in this paper have been submitted to Gene Expression Omnibus (http://www.ncbi.nlm.nih.gov/geo/) with accession number GSE107434. Other data including m^6A peak calling and annotation, FMRP targets, autism spectrum disorder-associated genes, differential gene expression analyses and overlap analyses are shown in (Supplementary Material, Tables S1–3). All other relevant data are available from the corresponding author. Command used to run Homer findPeaks is shown in (Supplementary Material, Table S1). Commands used to run Bowtie, IGV tools, Tophat, MeTPeak, MeTDiff, Cufflinks, Cuffdiff or MetaPlotR are included in the manuals of corresponding software, which are available on the internet. R code used to perform bioinformatics analyses is available upon request.

Supplementary Material

Supplementary Material is available at *HMG* online.

Acknowledgements

We thank Nirav Patel at Nonhuman Primate Genomics Core of Emory University/Yerkes National Primate Research Center for the assistance with high-throughput sequencing. pcDNA 3.0 with N-FLAG-tagged human YTHDF2 was a gift from Dr. Chuan He at the University of Chicago.

Conflict of Interest statement. None declared.

Funding

National Institutes of Health (NS051630, NS091859, NS079625 and MH102690 to P.J., HG008935 and NS097206 to P.J. and H.S., NS047344 to H.S.; GM122083 to H.W.); the Simons Foundation Autism Research Initiative (239320 to P.J. and 308988 to H.S.).

References

1. Wei, C.M., Gershowitz, A. and Moss, B. (1975) Methylated nucleotides block 5' terminus of HeLa cell messenger RNA. *Cell*, **4**, 379–386.
2. Liu, J., Yue, Y., Han, D., Wang, X., Fu, Y., Zhang, L., Jia, G., Yu, M., Lu, Z., Deng, X. *et al.* (2014) A METTL3-METTL14 complex mediates mammalian nuclear RNA N6-adenosine methylation. *Nat. Chem. Biol.*, **10**, 93–95.
3. Wang, X., Feng, J., Xue, Y., Guan, Z., Zhang, D., Liu, Z., Gong, Z., Wang, Q., Huang, J., Tang, C. *et al.* (2016) Structural basis of N(6)-adenosine methylation by the METTL3-METTL14 complex. *Nature*, **534**, 575–578.
4. Wang, P., Doxtader, K.A. and Nam, Y. (2016) Structural basis for cooperative function of Mettl3 and Mettl14 methyltransferases. *Mol. Cell*, **63**, 306–317.
5. Patil, D.P., Chen, C.K., Pickering, B.F., Chow, A., Jackson, C., Guttman, M. and Jaffrey, S.R. (2016) m(6)A RNA methylation promotes XIST-mediated transcriptional repression. *Nature*, **537**, 369–373.
6. Schwartz, S., Mumbach, M.R., Jovanovic, M., Wang, T., Maciag, K., Bushkin, G.G., Mertins, P., Ter-Ovanesyan, D., Habib, N., Cacchiarelli, D. *et al.* (2014) Perturbation of m6A writers reveals two distinct classes of mRNA methylation at internal and 5' sites. *Cell Rep.*, **8**, 284–296.
7. Jia, G., Fu, Y., Zhao, X., Dai, Q., Zheng, G., Yang, Y., Yi, C., Lindahl, T., Pan, T., Yang, Y.G. *et al.* (2011) N6-methyladenosine in nuclear RNA is a major substrate of the obesity-associated FTO. *Nat. Chem. Biol.*, **7**, 885–887.
8. Zheng, G., Dahl, J.A., Niu, Y., Fedorcsak, P., Huang, C.M., Li, C.J., Vagbo, C.B., Shi, Y., Wang, W.L., Song, S.H. *et al.* (2013) ALKBH5 is a mammalian RNA demethylase that impacts RNA metabolism and mouse fertility. *Mol. Cell*, **49**, 18–29.
9. Xiao, W., Adhikari, S., Dahal, U., Chen, Y.S., Hao, Y.J., Sun, B.F., Sun, H.Y., Li, A., Ping, X.L., Lai, W.Y. *et al.* (2016) Nuclear m(6)A reader YTHDC1 regulates mRNA splicing. *Mol. Cell*, **61**, 507–519.
10. Alarcon, C.R., Goodarzi, H., Lee, H., Liu, X., Tavazoie, S. and Tavazoie, S.F. (2015) HNRNPA2B1 is a mediator of m(6)A-dependent nuclear RNA processing events. *Cell*, **162**, 1299–1308.
11. Roundtree, I.A., Luo, G.Z., Zhang, Z., Wang, X., Zhou, T., Cui, Y., Sha, J., Huang, X., Guerrero, L., Xie, P. *et al.* (2017) YTHDC1 mediates nuclear export of N(6)-methyladenosine methylated mRNAs. *Elife*, **6**, e31311.
12. Alarcon, C.R., Lee, H., Goodarzi, H., Halberg, N. and Tavazoie, S.F. (2015) N6-methyladenosine marks primary microRNAs for processing. *Nature*, **519**, 482–485.
13. Wang, X., Zhao, B.S., Roundtree, I.A., Lu, Z., Han, D., Ma, H., Weng, X., Chen, K., Shi, H. and He, C. (2015) N(6)-methyladenosine modulates messenger RNA translation efficiency. *Cell*, **161**, 1388–1399.
14. Shi, H., Wang, X., Lu, Z., Zhao, B.S., Ma, H., Hsu, P.J., Liu, C. and He, C. (2017) YTHDF3 facilitates translation and decay of N6-methyladenosine-modified RNA. *Cell Res.*, **27**, 315–328.
15. Li, A., Chen, Y.S., Ping, X.L., Yang, X., Xiao, W., Yang, Y., Sun, H.Y., Zhu, Q., Baidya, P., Wang, X. *et al.* (2017) Cytoplasmic m6A reader YTHDF3 promotes mRNA translation. *Cell Res.*, **27**, 444–447.
16. Hsu, P.J., Zhu, Y., Ma, H., Guo, Y., Shi, X., Liu, Y., Qi, M., Lu, Z., Shi, H., Wang, J. *et al.* (2017) Ythdc2 is an N6-methyladenosine binding protein that regulates mammalian spermatogenesis. *Cell Res.*, **27**, 1115–1127.
17. Meyer, K.D., Patil, D.P., Zhou, J., Zinoviev, A., Skabkin, M.A., Elemento, O., Pestova, T.V., Qian, S.B. and Jaffrey, S.R. (2015) 5' UTR m(6)A promotes cap-independent translation. *Cell*, **163**, 999–1010.
18. Wang, X., Lu, Z., Gomez, A., Hon, G.C., Yue, Y., Han, D., Fu, Y., Parisien, M., Dai, Q., Jia, G. *et al.* (2014) N6-methyladenosine-dependent regulation of messenger RNA stability. *Nature*, **505**, 117–120.
19. Molinie, B., Wang, J., Lim, K.S., Hillebrand, R., Lu, Z.X., Van Wittenberghe, N., Howard, B.D., Daneshvar, K., Mullen, A.C., Dedon, P. *et al.* (2016) m(6)A-LAIC-seq reveals the census and complexity of the m(6)A epitranscriptome. *Nat. Methods*, **13**, 692–698.
20. Liu, N., Zhou, K.I., Parisien, M., Dai, Q., Diatchenko, L. and Pan, T. (2017) N6-methyladenosine alters RNA structure to regulate binding of a low-complexity protein. *Nucleic Acids Res.*, **45**, 6051–6063.
21. Liu, N., Dai, Q., Zheng, G., He, C., Parisien, M. and Pan, T. (2015) N(6)-methyladenosine-dependent RNA structural switches regulate RNA-protein interactions. *Nature*, **518**, 560–564.
22. Meyer, K.D., Saletore, Y., Zumbo, P., Elemento, O., Mason, C.E. and Jaffrey, S.R. (2012) Comprehensive analysis of mRNA methylation reveals enrichment in 3' UTRs and near stop codons. *Cell*, **149**, 1635–1646.
23. Dominissini, D., Moshitch-Moshkovitz, S., Schwartz, S., Salmon-Divon, M., Ungar, L., Osenberg, S., Cesarkas, K., Jacob-Hirsch, J., Amariglio, N., Kupiec, M. *et al.* (2012) Topology of the human and mouse m6A RNA methylomes revealed by m6A-seq. *Nature*, **485**, 201–206.
24. Hess, M.E., Hess, S., Meyer, K.D., Verhagen, L.A., Koch, L., Bronneke, H.S., Dietrich, M.O., Jordan, S.D., Saletore, Y., Elemento, O. *et al.* (2013) The fat mass and obesity associated gene (Fto) regulates activity of the dopaminergic midbrain circuitry. *Nat. Neurosci.*, **16**, 1042–1048.
25. Fustin, J.M., Doi, M., Yamaguchi, Y., Hida, H., Nishimura, S., Yoshida, M., Isagawa, T., Morioka, M.S., Kakeya, H., Manabe, I. *et al.* (2013) RNA-methylation-dependent RNA processing controls the speed of the circadian clock. *Cell*, **155**, 793–806.
26. Walters, B.J., Mercaldo, V., Gillon, C.J., Yip, M., Neve, R.L., Boyce, F.M., Frankland, P.W. and Josselyn, S.A. (2017) The role of the RNA demethylase FTO (Fat Mass and Obesity-associated) and mRNA methylation in hippocampal memory formation. *Neuropsychopharmacology*, **42**, 1502–1510.
27. Yoon, K.J., Ringeling, F.R., Vissers, C., Jacob, F., Pokrass, M., Jimenez-Cyrus, D., Su, Y., Kim, N.S., Zhu, Y., Zheng, L. *et al.* (2017) Temporal control of mammalian cortical neurogenesis by m6A methylation. *Cell*, **171**, 877–889.
28. Li, L., Zang, L., Zhang, F., Chen, J., Shen, H., Shu, L., Liang, F., Feng, C., Chen, D., Tao, H. *et al.* (2017) Fat mass and obesity-associated (FTO) protein regulates adult neurogenesis. *Hum. Mol. Genet.*, **26**, 2398–2411.
29. Santoro, M.R., Bray, S.M. and Warren, S.T. (2012) Molecular mechanisms of fragile X syndrome: a twenty-year perspective. *Annu. Rev. Pathol.*, **7**, 219–245.
30. Kelleher, R.J. 3rd and Bear, M.F. (2008) The autistic neuron: troubled translation? *Cell*, **135**, 401–406.

31. Wang, L.W., Berry-Kravis, E. and Hagerman, R.J. (2010) Fragile X: leading the way for targeted treatments in autism. *Neurotherapeutics*, **7**, 264–274.
32. Verkerk, A.J., Pieretti, M., Sutcliffe, J.S., Fu, Y.H., Kuhl, D.P., Pizzuti, A., Reiner, O., Richards, S., Victoria, M.F., Zhang, F.P. *et al.* (1991) Identification of a gene (FMR-1) containing a CGG repeat coincident with a breakpoint cluster region exhibiting length variation in fragile X syndrome. *Cell*, **65**, 905–914.
33. Stefani, G., Fraser, C.E., Darnell, J.C. and Darnell, R.B. (2004) Fragile X mental retardation protein is associated with translating polyribosomes in neuronal cells. *J. Neurosci.*, **24**, 7272–7276.
34. Khandjian, E.W., Huot, M.E., Tremblay, S., Davidovic, L., Mazroui, R. and Bardoni, B. (2004) Biochemical evidence for the association of fragile X mental retardation protein with brain polyribosomal ribonucleoparticles. *Proc. Natl. Acad. Sci. USA*, **101**, 13357–13362.
35. Feng, Y., Absher, D., Eberhart, D.E., Brown, V., Malter, H.E. and Warren, S.T. (1997) FMRP associates with polyribosomes as an mRNP, and the I304N mutation of severe fragile X syndrome abolishes this association. *Mol. Cell*, **1**, 109–118.
36. Darnell, J.C., Van Driesche, S.J., Zhang, C., Hung, K.Y., Mele, A., Fraser, C.E., Stone, E.F., Chen, C., Fak, J.J., Chi, S.W. *et al.* (2011) FMRP stalls ribosomal translocation on mRNAs linked to synaptic function and autism. *Cell*, **146**, 247–261.
37. Ascano, M. Jr., Mukherjee, N., Bandaru, P., Miller, J.B., Nusbaum, J.D., Corcoran, D.L., Langlois, C., Munschauer, M., Dewell, S., Hafner, M. *et al.* (2012) FMRP targets distinct mRNA sequence elements to regulate protein expression. *Nature*, **492**, 382–386.
38. Anderson, B.R., Chopra, P., Suhl, J.A., Warren, S.T. and Bassell, G.J. (2016) Identification of consensus binding sites clarifies FMRP binding determinants. *Nucleic Acids Res.*, **44**, 6649–6659.
39. Edupuganti, R.R., Geiger, S., Lindeboom, R.G.H., Shi, H., Hsu, P.J., Lu, Z., Wang, S.-Y., Baltissen, M.P.A., Jansen, P.W.T.C., Rossa, M. *et al.* (2017) N6-methyladenosine (m6A) recruits and repels proteins to regulate mRNA homeostasis. *Nat. Struct. Mol. Biol.*, **24**, 870–878.
40. Dominissini, D., Moshitch-Moshkovitz, S., Salmon-Divon, M., Amariglio, N. and Rechavi, G. (2013) Transcriptome-wide mapping of N(6)-methyladenosine by m(6)A-seq based on immunocapturing and massively parallel sequencing. *Nat. Protoc.*, **8**, 176–189.
41. Chang, M., Lv, H., Zhang, W., Ma, C., He, X., Zhao, S., Zhang, Z.W., Zeng, Y.X., Song, S., Niu, Y. *et al.* (2017) Region-specific RNA m(6)A methylation represents a new layer of control in the gene regulatory network in the mouse brain. *Open Biol.*, **7**, 170166.
42. Cui, X., Meng, J., Zhang, S., Chen, Y. and Huang, Y. (2016) A novel algorithm for calling mRNA m6A peaks by modeling biological variances in MeRIP-seq data. *Bioinformatics*, **32**, i378–i385.
43. Cui, X., Zhang, L., Meng, J., Rao, M., Chen, Y. and Huang, Y. (2015) MeTDiff: a novel differential RNA methylation analysis for MeRIP-Seq data. *IEEE/ACM Trans. Comput. Biol. Bioinform.*, **15**, 526–534.
44. Du, H., Zhao, Y., He, J., Zhang, Y., Xi, H., Liu, M., Ma, J. and Wu, L. (2016) YTHDF2 destabilizes m(6)A-containing RNA through direct recruitment of the CCR4-NOT deadenylase complex. *Nat. Commun.*, **7**, 12626.
45. Ke, S., Alemu, E.A., Mertens, C., Gantman, E.C., Fak, J.J., Mele, A., Haripal, B., Zucker-Scharff, I., Moore, M.J., Park, C.Y. *et al.* (2015) A majority of m6A residues are in the last exons, allowing the potential for 3' UTR regulation. *Genes Dev.*, **29**, 2037–2053.
46. Wang, Y., Li, Y., Toth, J.I., Petroski, M.D., Zhang, Z. and Zhao, J.C. (2014) N6-methyladenosine modification destabilizes developmental regulators in embryonic stem cells. *Nat. Cell. Biol.*, **16**, 191–198.
47. Ashley, C.T. Jr., Wilkinson, K.D., Reines, D. and Warren, S.T. (1993) FMR1 protein: conserved RNP family domains and selective RNA binding. *Science*, **262**, 563–566.
48. Myrick, L.K., Hashimoto, H., Cheng, X. and Warren, S.T. (2015) Human FMRP contains an integral tandem Agenet (Tudor) and KH motif in the amino terminal domain. *Hum. Mol. Genet.*, **24**, 1733–1740.
49. Fu, Y., Dominissini, D., Rechavi, G. and He, C. (2014) Gene expression regulation mediated through reversible m(6)A RNA methylation. *Nat. Rev. Genet.*, **15**, 293–306.
50. Richter, J.D., Bassell, G.J. and Klann, E. (2015) Dysregulation and restoration of translational homeostasis in fragile X syndrome. *Nat. Rev. Neurosci.*, **16**, 595–605.
51. Aakalu, G., Smith, W.B., Nguyen, N., Jiang, C. and Schuman, E.M. (2001) Dynamic visualization of local protein synthesis in hippocampal neurons. *Neuron*, **30**, 489–502.
52. Zalfa, F., Eleuteri, B., Dickson, K.S., Mercaldo, V., De Rubeis, S., di Penta, A., Tabolacci, E., Chiurazzi, P., Neri, G., Grant, S.G. *et al.* (2007) A new function for the fragile X mental retardation protein in regulation of PSD-95 mRNA stability. *Nat. Neurosci.*, **10**, 578–587.
53. Zhang, M., Wang, Q. and Huang, Y. (2007) Fragile X mental retardation protein FMRP and the RNA export factor NXF2 associate with and destabilize Nxf1 mRNA in neuronal cells. *Proc. Natl. Acad. Sci. USA*, **104**, 10057–10062.
54. Yu, J., Chen, M., Huang, H., Zhu, J., Song, H., Park, J. and Ji, S.J. (2018) Dynamic m6A modification regulates local translation of mRNA in axons. *Nucleic Acids Res.*, **46**, 1412–1423.
55. Hernandez, R.N., Feinberg, R.L., Vaurio, R., Passanante, N.M., Thompson, R.E. and Kaufmann, W.E. (2009) Autism spectrum disorder in fragile X syndrome: a longitudinal evaluation. *Am. J. Med. Genet. A*, **149a**, 1125–1137.
56. Schindelin, J., Arganda-Carreras, I., Frise, E., Kaynig, V., Longair, M., Pietzsch, T., Preibisch, S., Rueden, C., Saalfeld, S., Schmid, B. *et al.* (2012) Fiji: an open-source platform for biological-image analysis. *Nat. Methods*, **9**, 676–682.
57. Zhang, F., Hammack, C., Ogden, S.C., Cheng, Y., Lee, E.M., Wen, Z., Qian, X., Nguyen, H.N., Li, Y., Yao, B. *et al.* (2016) Molecular signatures associated with ZIKV exposure in human cortical neural progenitors. *Nucleic Acids Res.*, **44**, 8610–8620.
58. Myrick, L.K., Nakamoto-Kinoshita, M., Lindor, N.M., Kirmani, S., Cheng, X. and Warren, S.T. (2014) Fragile X syndrome due to a missense mutation. *Eur. J. Hum. Genet.*, **22**, 1185–1189.
59. Brown, V., Jin, P., Ceman, S., Darnell, J.C., O'Donnell, W.T., Tenenbaum, S.A., Jin, X., Feng, Y., Wilkinson, K.D., Keene, J.D. *et al.* (2001) Microarray identification of FMRP-associated brain mRNAs and altered mRNA translational profiles in fragile X syndrome. *Cell*, **107**, 477–487.
60. Langmead, B. and Salzberg, S.L. (2012) Fast gapped-read alignment with Bowtie 2. *Nat. Methods*, **9**, 357–359.
61. Heinz, S., Benner, C., Spann, N., Bertolino, E., Lin, Y.C., Laslo, P., Cheng, J.X., Murre, C., Singh, H. and Glass, C.K. (2010) Simple combinations of lineage-determining transcription factors prime cis-regulatory elements required for macrophage and B cell identities. *Mol. Cell*, **38**, 576–589.
62. Robinson, J.T., Thorvaldsdottir, H., Winckler, W., Guttman, M., Lander, E.S., Getz, G. and Mesirov, J.P. (2011) Integrative genomics viewer. *Nat. Biotechnol.*, **29**, 24–26.

63. Thorvaldsdottir, H., Robinson, J.T. and Mesirov, J.P. (2013) Integrative Genomics Viewer (IGV): high-performance genomics data visualization and exploration. *Brief Bioinform.*, **14**, 178–192.
64. Bailey, T.L. (2011) DREME: motif discovery in transcription factor ChIP-seq data. *Bioinformatics*, **27**, 1653–1659.
65. Bailey, T.L. and Machanick, P. (2012) Inferring direct DNA binding from ChIP-seq. *Nucleic Acids Res.*, **40**, e128.
66. Kim, D., Pertea, G., Trapnell, C., Pimentel, H., Kelley, R. and Salzberg, S.L. (2013) TopHat2: accurate alignment of transcriptomes in the presence of insertions, deletions and gene fusions. *Genome Biol.*, **14**, R36.
67. Trapnell, C., Williams, B.A., Pertea, G., Mortazavi, A., Kwan, G., van Baren, M.J., Salzberg, S.L., Wold, B.J. and Pachter, L. (2010) Transcript assembly and quantification by RNA-Seq reveals unannotated transcripts and isoform switching during cell differentiation. *Nat. Biotechnol.*, **28**, 511–515.
68. Trapnell, C., Hendrickson, D.G., Sauvageau, M., Goff, L., Rinn, J.L. and Pachter, L. (2013) Differential analysis of gene regulation at transcript resolution with RNA-seq. *Nat. Biotechnol.*, **31**, 46–53.
69. Olarerin-George, A.O. and Jaffrey, S.R. (2017) MetaPlotR: a Perl/R pipeline for plotting metagenes of nucleotide modifications and other transcriptomic sites. *Bioinformatics*, **33**, 1563–1564.
70. Quinlan, A.R. and Hall, I.M. (2010) BEDTools: a flexible suite of utilities for comparing genomic features. *Bioinformatics*, **26**, 841–842.
71. Yang, Y.C., Di, C., Hu, B., Zhou, M., Liu, Y., Song, N., Li, Y., Umetsu, J. and Lu, Z.J. (2015) CLIPdb: a CLIP-seq database for protein-RNA interactions. *BMC Genomics*, **16**, 51.
72. Uren, P.J., Bahrami-Samani, E., Burns, S.C., Qiao, M., Karginov, F.V., Hodges, E., Hannon, G.J., Sanford, J.R., Penalva, L.O. and Smith, A.D. (2012) Site identification in high-throughput RNA-protein interaction data. *Bioinformatics*, **28**, 3013–3020.
73. Huang da, W., Sherman, B.T. and Lempicki, R.A. (2009) Systematic and integrative analysis of large gene lists using DAVID bioinformatics resources. *Nat. Protoc.*, **4**, 44–57.
74. Wang, J., Duncan, D., Shi, Z. and Zhang, B. (2013) WEB-based GEne SeT AnaLysis Toolkit (WebGestalt): update 2013. *Nucleic Acids Res.*, **41**, W77–W83.